CHEMISTRY OF MATERIALS

pubs.acs.org/cm

Article

Electrochemical Denitrification and Oxidative Dehydrogenation of Ethylbenzene over N-doped Mesoporous Carbon: Atomic Level Understanding of Catalytic Activity by ^{15}N NMR Spectroscopy

Ireneusz Szewczyk, Anna Rokicińska, Marek Michalik, Jianhong Chen, Aleksander Jaworski, Rihards Aleksis, Andrew J. Pell, Niklas Hedin, Adam Slabon,* and Piotr Kuśtrowski*

Cite This: *Chem. Mater.* 2020, 32, 7263−7273

Read Online

ACCESS | Metrics & More | Article Recommendations

ABSTRACT: Spherical mesoporous carbon (with a particle size in the range of 40−75 μm) was synthesized by nanoreplication of a hard silica template using sucrose as the carbon precursor. The mesoporous carbon with BET surface areas higher than 1200 m^2/g was doped with N by a treatment in an aqueous solution of nitric acid and/or in a flow of gaseous ammonia. The highest N content (3.2 wt % of N in bulk) was obtained when both modification methods were combined. Complementary physicochemical characterization techniques, including scanning electron microscopy (SEM), low-temperature N_2 adsorption, powder X-ray diffraction (XRD), and Raman spectroscopy revealed the morphology, structure, and textural properties of the synthesized N-loaded carbon materials. For the identification of the detailed chemical structure on the surface of the carbons, ^{1}H, ^{13}C, and ^{15}N solid-state nuclear magnetic resonance (NMR) measurements were performed, and the data were supported by chemical shift calculations with accurate quantum chemistry methods and X-ray photoelectron spectroscopic (XPS) analyses. All NMR experiments were performed at natural isotope abundance. The verified experimental data clearly showed that after the introduction of the N-containing moieties by the combined methods of treatment, a high concentration of pyridinic N at the edge, and pyrrolic N being external to the edge, was achieved for the mesoporous carbon. The distributed N surface species promoted the catalytic activity in the oxidative dehydrogenation of ethylbenzene to styrene but did not significantly influence the efficiency of the carbon materials in the electrochemical reduction of nitrate ions.

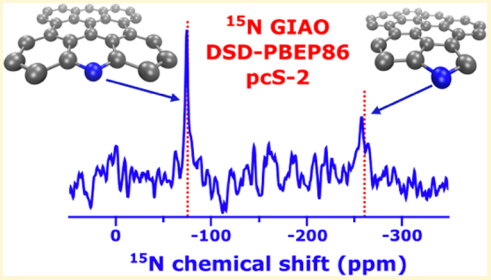

INTRODUCTION

Carbon-based materials have been implemented in a wide range of applications (such as adsorption,[1,2] electrochemistry[3−9] and catalysis[10−12]) for a long time due to their specific properties including structure, porosity, surface composition, and conductivity. In catalytic processes, activated carbons still play a dominant role as the active phase and/or support, while graphene, graphene oxide, and carbon nanotubes (CNTs) have gained increasingly large interest in the research community.[3,13−15] In the late 1990s, Ryoo et al.[16] developed a new approach for a formation of carbons with a well-controlled mesoporosity. Such materials are produced as negative replicas of silica-type hard templates. After infiltrating a carbon precursor (e.g., sucrose) in a porous system of a SiO_2 matrix, the resulting composite is carbonized and treated with a NaOH or HF solution to remove the inorganic template. Depending on the pore size and wall arrangement in the silica matrix, carbon materials with various pore architecture are obtained.[6,17−19]

Doping of carbon with other nonmetals results in the formation of different organic functionalities containing most often oxygen,[15,18−21] nitrogen,[3,8,20,22−24] or sulfur.[25,26] The incorporation of heteroatoms into the carbon structure is based on two possible strategies: (i) decomposition of a carbon precursor (e.g., composite, polymer) containing nonmetal atoms (bottom-up approach)[10,17] or (ii) postsynthetic activation of a carbon material using a heteroatom-containing modifier (top-down approach).[27,28] Development of various, optimal pathways for the modification with noncarbon species as well as properties of the doped materials is the subject of an increasing number of studies, because the formed functional groups are vital in a variety of applications. Metal-free carbon materials can be considered green catalysts with respect to their ease of recycling and work efficiently in some catalytic processes, such as oxidative dehydrogenation of alkanes,[15,17,24,29,30] where oxygen-containing species located at

Received: April 19, 2020
Revised: July 31, 2020
Published: August 3, 2020

https://dx.doi.org/10.1021/acs.chemmater.0c01666
Chem. Mater. 2020, 32, 7263−7273

the edges of graphitic plates are commonly considered to be active sites in an oxidative atmosphere.[19,21,31] On the other hand, some nitrogen-containing groups, for example pyridinic ones, show activity in acid−base catalysis,[13] oxygen reduction reactions (ORR),[3−5,7,8] and other electro-transfer processes.[25,32] Nevertheless, a controlled distribution of heteroatom-containing groups in mesoporous carbon materials remains a big challenge, as their form and stability strongly depends on the temperature, the nature of the heteroatoms, and the state of the starting carbon material even when model substrates (e.g., graphene, graphene oxides) are used.[22,33] Combining more than one heteroatom can create heterogeneous groups (like amides) and also induce interactions between surface groups that influence the electrophilicity and electron transfer on the surface of the catalyst.[17,28] It has been observed that by introducing various amounts of N- and O-containing species, the basicity is influenced, which in turn could be important for the CO_2 adsorption.[34] Seo et al.[33] studied a doped reduced graphene oxide material with an optical band gap of 1.7−2.1 eV with implicatively stable N (pyridinic) and O (C═O) surroundings. Electronic synergy also concerns adsorbed molecules, therefore charge generated during the ORR process might be channeled efficiently.[24,33] Similar interactions occur in the case of other nonmetal pairs such as nitrogen doped with phosphorus[20,35] or boron.[36] In addition, with oxygen atoms being connected to high-oxidation-state atoms, the deactivation of the active site has been shown to be prevented by Ternero-Hidalgo et al.[35]

In this work, we discuss the impact of oxygen- and nitrogen-containing groups on the surface of sucrose-derived mesoporous carbon replicas on the performance in the electrochemical nitrate reduction, and the oxidative dehydrogenation of ethylbenzene. We propose two approaches to generate heteroatom-containing groups based on treating the replica with (i) a HNO_3 solution and/or (ii) gaseous NH_3. Especially interesting, original results are obtained by combining the above-mentioned ways, which leads to the formation of nitro moieties (after soaking in the HNO_3 solution) and their subsequent reduction in NH_3 at an elevated temperature. X-ray photoelectron spectroscopy (XPS) and ^{15}N solid-state nuclear magnetic resonance (^{15}N NMR) are used to describe the chemical state of the modified carbon surfaces and to conclude how these modifications influence the catalytic and electrochemical activity. The use of the ^{15}N solid-state NMR without isotopic labeling is very promising for further studies as costly ^{15}N isotope labeling can be circumvented.[37,38]

EXPERIMENTAL SECTION

Synthesis. Spherical silica gel (40−75 μm particle size, Supelco) and an acidified sucrose solution (with the H_2O/sugar/H_2SO_4 mass ratio of 50.0/12.5/1.4) were used in the synthesis of the starting carbon replica as a carbon source and a template, respectively. Precisely, 1.0 g of SiO_2 (dried initially at 120 °C for 1 h) was impregnated using the incipient wetness technique with a solution volume containing 1.7 g of sucrose. The obtained composite was placed in an oven at 100 °C for 6 h, then the temperature was raised to 160 °C for another 6 h. The procedure of impregnation and heating was repeated using the same sucrose solution, 1.6 g of sucrose per 1.0 g of the sample. The material was carbonized in a tubular furnace under a N_2 flow (40 cm^3/min) at 650 °C with a heating rate of 1 °C/min and an isothermal period of 4 h. Finally, the silica template was removed by double washing with a HF solution (5 wt %, room temperature). The produced carbon replica with a negligible amount of the remaining SiO_2 template below 1 wt % (denoted as S0) was isolated, washed with distilled water and ethanol (96%), and dried overnight (50 °C).

A part of the S0 sample was oxidized by contact with an aqueous solution of HNO_3 (40 wt %), at 1.0 g of S0 per 10 cm^3 of the HNO_3 solution at 50 °C for 3 h. The resulting product (denoted as SK) was filtered, washed with distilled water until reaching neutral pH, and dried overnight at 50 °C.

Both S0 and SK were modified in the presence of gaseous NH_3 at an elevated temperature. An amount of 100 mg of the sample was placed on a quartz wool plug in a quartz flow microreactor. The material was pretreated under a N_2 atmosphere (50 cm^3/min) at 250 °C for 30 min. Then, temperature increased to 500 °C, and the N_2 flow was changed to a NH_3/He mixture (20 vol % of NH_3, total flow rate = 30 cm^3/min). The modification lasting for 1 h resulted in obtaining the samples marked S0_N and SK_N, respectively.

N_2 Adsorption. N_2 adsorption measurements were performed for outgassed samples (dynamic vacuum, 250 °C, 4 h) at −196 °C in an ASAP 2020 instrument (Micrometrics). The obtained data were analyzed using the following models: Brunauer−Emmett−Teller (specific surface area, S_{BET}), t-plot (micropore volume, V_{micro}), Barret−Joyner−Halenda (pore size distribution and mesopore volume, V_{meso}), and single point at $p/p_0 \sim 0.99$ (total pore volume, V_{total}).

Powder X-ray Diffraction (XRD). XRD patterns were collected using Cu Kα radiation (1.54184 Å) with a Bruker D2 Phaser diffractometer equipped with a LYNXEYE detector within a 2θ range of 10−60° using a step of 0.02°.

Raman Spectroscopy. Raman spectra were recorded on a LabRAM HR 800 spectrometer equipped with an 800 nm focal length spectrograph. A back thinned CCD detector with 1024 × 256 pixels and a spectral range of 200−1050 nm was air cooled at −70 °C. An air cooled double frequency Nd:YAG laser (532 nm/50 mW), edge, and interference filters for measurements <100 cm^{-1} were used. The laser intensity was adjusted by a software controlled filter wheel with 6ND filters. The baselines were fitted by a second derivative method with adjacent averaging smoothing. To create the baseline for all samples, 16 spots of each sample with intensity below 500 were chosen to assign the baseline with the interpolation method of the spline.

Scanning Electron Microscopy (SEM). SEM images were taken on a HITACHI S-4700 field emission microscope at an accelerating voltage of 20 kV. Samples were prepared by mounting powder onto a conducting adhesive carbon disc. In order to reduce charging, the materials were coated with a Au layer.

Elemental Analysis. The chemical composition of the carbon materials (content of C, N, and H) was determined in a FLASH 2000 elemental analyzer (Thermo Scientific) equipped with a thermal conductivity detector (TCD), and an autosampler. Quantitative analysis on the metal content was performed by inductively coupled plasma optical emission spectrometry (ICP-OES).

X-ray Photoelectron Spectroscopy. XPS measurements were performed in a Prevac photoelectron spectrometer equipped with a hemispherical analyzer (VG SCIENTA R3000). The spectra were taken using a monochromatized aluminum source Al K_α (E = 1486.6 eV). The base pressure in the analytical chamber was 5 × 10^{-9} mbar. The binding energy scale was calibrated using the Au 4f reference peak at 84.0 eV. The surface composition was analyzed taking into account the areas and binding energies of C 1s, O 1s, and N 1s core levels. The spectra were fitted and deconvoluted using the CasaXPS software.

Solid-State Nuclear Magnetic Resonance. All magic-angle-spinning (MAS) NMR experiments were performed at a magnetic field of 14.1 T (Larmor frequencies of 600.12, 150.92, and 60.83 MHz for ^1H, ^{13}C, and ^{15}N, respectively) on a Bruker Avance-III spectrometer. ^1H MAS and ^1H−^{13}C heteronuclear correlation (HETCOR) NMR spectra were recorded with a 1.3 mm probehead and 60 kHz MAS rate. Proton acquisitions involved a rotor-synchronized, double-adiabatic spin−echo sequence with a 90° excitation pulse of 1.25 μs followed by a pair of 50.0 μs tanh/tan short high-power adiabatic pulses (SHAPs) with a 5 MHz frequency

https://dx.doi.org/10.1021/acs.chemmater.0c01666
Chem. Mater. 2020, 32, 7263−7273

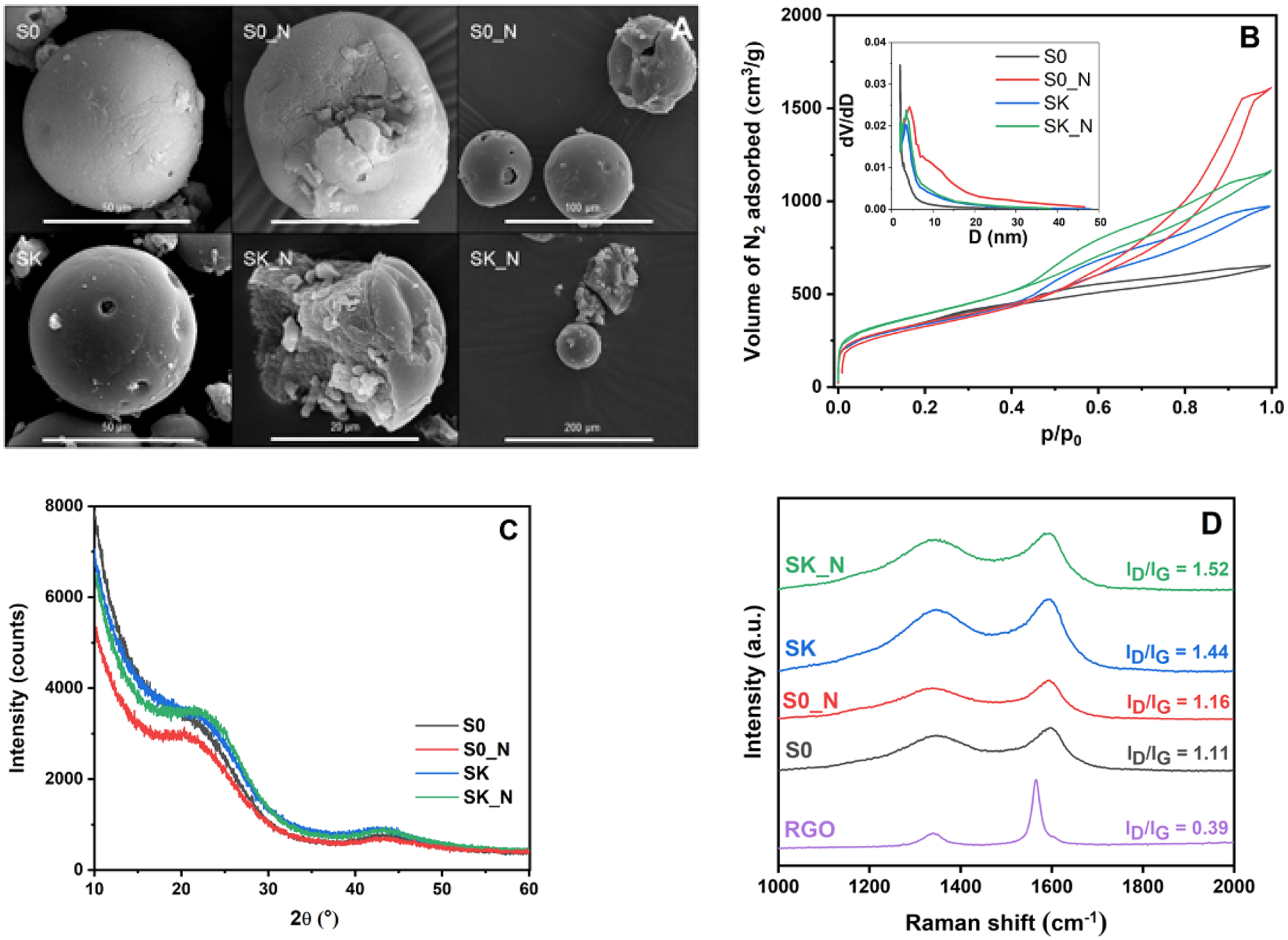

Figure 1. SEM images (A), N_2 adsorption−desorption isotherms with BJH pore size distribution (B), XRD patterns (C), and Raman spectra (D) collected for the pristine and modified mesoporous carbon replicas. S0, SK, S0_N, and SK_N stand for unmodified carbon replica, carbon replica treated with HNO_3, carbon replica treated with NH_3, and carbon replica treated first with HNO_3 and then NH_3.

sweep.[39,40] This pulse sequence was used to suppress the proton background signal and obtain a flat baseline in the spectra. All pulses operated at a nutation frequency of 200 kHz. 128 signal transients with a 1 s relaxation delay were collected. The $^{1}H-^{13}C$ HETCOR experiment involved Hartmann−Hahn matched ^{1}H and ^{13}C radio frequency fields of 20 and 40 kHz, respectively, a 1 ms contact interval for the cross-polarization step, 80 kHz SPINAL-64 ^{1}H decoupling, and 5616 scans with a 1 s relaxation delay collected for each t_1 point. The ^{1}H and ^{13}C chemical shifts were referenced with respect to tetramethylsilane (TMS). Directly excited ^{13}C and ^{15}N MAS NMR spectra were recorded with the single-pulse ("Bloch-decay") protocol using a 7 mm probehead and 7 kHz MAS rate. The ^{13}C and ^{15}N acquisitions involved 4.0 and 6.0 μs excitation pulses with nutation frequencies of 63 and 38 kHz, 9216 and 466 944 signal transients collected with recycle delays of 25 and 1 s, respectively, and no proton decoupling. The ^{15}N NMR chemical shifts are reported with respect to nitromethane. All NMR experiments were performed at natural isotope abundance.

Chemical Shifts Calculations. All calculations were performed with the ORCA code version 4.1.2.[41] using a tight convergence tolerance of 1×10^{-8} Hartree. Models of different nitrogen in the carbon structure were obtained by geometry optimization with dispersion-corrected DFT at the level of the OLYP-D3(BJ) approximation[42−45] using a segmented, polarization consistent pc-2 basis set.[46] ^{13}C and ^{15}N nuclear shieldings were calculated at the level of perturbatively corrected DFT with the DSD-PBEP86 approximation[47] and a segmented pcS-2 basis set[48] with all electrons included in correlation (no frozen core). The GIAO approach with the RIJCOSX approximation was employed using Coulomb-fitting def2/J[49] and cc-pwCVTZ/C[50] auxiliary basis sets for the SCF and MP2 steps, respectively, and accurate grid settings for exchange integrals tested. Calculated ^{13}C and ^{15}N isotropic nuclear shieldings $[\sigma_{iso}=(\sigma_{xx} + \sigma_{yy} + \sigma_{zz})/3]$ were converted to ^{13}C and ^{15}N NMR isotropic chemical shifts (δ_{iso}) using CO_2 and N_2 molecules in the gas phase as secondary references at 125.0 and −75.3 ppm, respectively,[51,52] according to $\delta_{iso} = \sigma_{iso,\,ref} - \sigma_{iso}$. Reported chemical shift anisotropy (CSA) follows the Haeberlen convention: $\delta_{aniso} = \delta_{zz} - \delta_{iso}$ where $|\delta_{zz} - \delta_{iso}| \geq |\delta_{xx} - \delta_{iso}| \geq |\delta_{yy} - \delta_{iso}|$ and asymmetry parameter $\eta = (\delta_{xx} - \delta_{yy})/(\delta_{zz} - \delta_{iso})$.

Electrochemical Measurements. For preparation of electrodes, a mixture of N-doped carbon and Nafion (D-520 dispersion 5% w/w in water and 1-propanol, Alfa Aesar) was deposited on a surface of carbon fiber support (Quintech TP-030). A precursor solution was prepared by dissolving N-doped carbon (5 mg) in 30 μL of Nafion and 970 μL of ethanol (≥99%, VWR Chemicals). The mixture was dispersed by an Ultrasonic Cleaner (USC 300T, VWR) for 3 min. Then, 200 μL of the uniform mixture was dropped on each side of carbon substrate and dried at room temperature for 1 h. For the preparation of the electrolyte for electrochemical nitrate reduction, $NaNO_3$ (≥99.0%, Sigma-Aldrich) and Na_2SO_4 (99.0−100.5 wt %, Honeywell Fluka) were dissolved in water purified with a Milli-Q system (18.3 MΩ cm). A platinum wire and a 1 M Ag/AgCl electrode were used as a counter and reference electrode, respectively. The concentration of nitrate was analyzed by the procedure described by Robarge et al.[53] The amount of nitrite was determined with a Merck Spectroquant 114773 test kit (Merck KGaA), and NH_3 was analyzed by means of the Nessler method.[54]

https://dx.doi.org/10.1021/acs.chemmater.0c01666
Chem. Mater. 2020, 32, 7263−7273

Catalytic Tests. Catalytic activity was tested in the oxidative dehydrogenation of ethylbenzene (EB) using a quartz microreactor filled with 50 mg of a carbon sample placed on a quartz wool. A flow rate of gaseous reactants was controlled by mass flow controllers (Brooks 4800) to obtain a total flow rate of 50 cm^3/min (0.4 cm^3 of O_2 + 49.6 cm^3 of He, O_2/EB molar ratio = 1:1). The EB vapor was introduced into the reaction mixture by passing it through a pure liquid of EB being kept at a constant temperature of 25 °C. The reaction products were transferred directly to a gas chromatograph (Bruker 450-GC) via a six-port valve with heated lines and there analyzed. The instrument was equipped with three packed columns (Porapak Q, Molecular Sieve 5A, and Chromosorb W-HP) and three detectors (two flame ionization detectors—one coupled with a catalytic methanizer—and a thermal conductivity detector). Prior to a catalytic test, a sample was outgassed in a flow of He (50 cm^3/min) at 200 °C for 30 min. The temperature of the catalyst bed was then increased to 350 °C, and the dosing of the catalytic mixture began. The first GC analysis was initialized after 15 min of time-on-stream. The products were analyzed in intervals of 46 min during a total reaction time of 8 h. The catalytic performance was expressed as conversion of EB (C_{EB}), yield of i product (Y_i), and selectivity toward i product (S_i) using the following equations:

$$C_{EB} = \frac{F_{EB,0} - F_{EB}}{F_{EB,0}} \times 100$$

$$Y_i = \frac{F_i}{F_{EB,0}} \times 100$$

$$S_i = \frac{Y_i}{C_{EB}} \times 100$$

where $F_{EB,0}$ and F_{EB} are the molar flow rates of EB in inlet and outlet streams, whereas F_i is the molar flow rate of EB being transformed into the i product.

RESULTS AND DISCUSSION

Structure and Texture. To synthesize the parent mesoporous carbon, a commercially available spherical silica gel was used as the hard template, which was modified by a simple impregnation method using an aqueous solution of sucrose as an inexpensive carbon precursor. This facile route led to the obtaining of a carbon replica with a completely preserved spherical shape, as is shown by the SEM images in Figure 1A. Further modification of the carbon replica using a HNO_3 solution resulted in numerous and relatively wide craters being formed in the spherical particles. With treatment with gaseous NH_3 at elevated temperatures, even deeper pits were observed. The surfaces of the carbon particles were significantly cracked and crushed in the case of pretreatment with HNO_3 (for the sample SK_N). The destructed and cracked spheres can be greatly advantageous for the catalytic performance, because they provide an additional macrochannel system in the grain volume, opening access to the narrower micro- and mesopores being located in the interior of the particle. Accordingly, a carbonaceous material with a multimodal porosity is formed.

The increased accessibility to the pore system was confirmed by the results of low-temperature N_2 adsorption (cf. Figure 1B and Table 1). The starting material S0 exhibited a type IV isotherm characteristic of mesoporous solids and a specific surface area above 1200 m^2/g. Nevertheless, further activation of the S0 sample in both the HNO_3 solution and at the NH_3 atmosphere resulted in the opening of wider pores (meso- and macropores), which was manifested by a clear increase in the amount of adsorbed N_2 at high relative pressures p/p_0 and an appearance of corresponding maxima in the pore size distributions. The activated materials were characterized by a very large volume of mesopores and intraparticle voids (even as high as 2.52 cm^3/g for S0_N) and expanded S_{BET} (exceeding 1400 m^2/g after the treatment with NH_3).

Table 1. Bulk N Content and Textural Parameters of the Pristine and Modified Mesoporous Carbon Replicas

sample[a]	N content [wt %]	S_{BET} [m^2/g]	V_{micro} [cm^3/g]	V_{meso} [cm^3/g]	V_{total} [cm^3/g]
S0		1239	0.01	0.52	1.01
S0_N	0.6	1490	0.04	2.03	2.56
SK	2.0	1205	0.01	1.15	1.51
SK_N	3.2	1415	0.01	1.33	1.80

[a]S0, SK, S0_N, and SK_N stand for unmodified carbon replica, carbon replica treated with HNO_3, carbon replica treated with NH_3, and carbon replica treated first with HNO_3 and then NH_3.

The structural ordering of the materials was analyzed by XRD (Figure 1C). The collected XRD patterns show distinct, but rather broad, features at ca. 23° and 43° corresponding to the (002) and (101) reflections typical of a poorly ordered graphite structure. However, Raman spectroscopy was a more informative way to study features of the carbon structure of the studied materials (Figure 1D). Two featured bands at 1340 and 1590 cm^{-1} were observed and assigned as the D and G bands, respectively. The D band arises from the disordered sp^2 hybridized carbon, while the G band is associated with crystalline graphitic carbon.[55] Meanwhile, the intensity ratio of the D band and G band (I_D/I_G) is adopted to evaluate the graphitization degree of porous carbon materials.[56] The I_D/I_G ratios for all N-modified materials were higher than that of S0 (1.11) and the reference reduced graphene oxide (RGO, 0.39), but also higher than the N-doped porous carbon prepared from a N-containing zeolitic imidazolate framework with comparable and even higher nitrogen concentration, which has been indicative of the introduction of defects and disordered structures possibly being beneficial to applications in catalysis and electrochemistry.[57,58]

For both S0 and SK_N samples, the purity was confirmed by quantitative determination of the metal content by means of ICP-OES, which showed concentrations below 10 ppm for Co, Cr, Cu, Mn, Mo, Ni, V, W, Pd, and Pt.

Surface Functionalities. The chemical surface compositions of the studied materials were determined by XPS (Table 2). Since carbon, oxygen, and nitrogen were the only elements identified, the quantitative analysis was based on the C 1s, O 1s, and N 1s regions.

The sample treated with NH_3 (S0_N) had 0.7 atom % of nitrogen, and that treated with HNO_3 (SK), 2.6 atom % of nitrogen. Simultaneously, a significant increase in the oxygen content was observed with the HNO_3 treatment, while the NH_3 treatment reduced the oxygen content. The reduced amount of oxygen was linked to the reducing properties of NH_3.[59] The comparison of N/C mass ratios determined by elemental analysis and XPS revealed that all studied samples have evenly distributed N-containing functional groups throughout the whole volume.

More detailed results were obtained by deconvolution of the XPS O 1s and N 1s spectra, which provided evidence for several different O and N species being distributed on the carbon-rich surfaces (Figure 2). In the N 1s core region, four main components at 398.9 eV (±0.1 eV), 400.2 eV (±0.1 eV),

https://dx.doi.org/10.1021/acs.chemmater.0c01666
Chem. Mater. 2020, 32, 7263−7273

Table 2. Content of O and N in Particular Functionalities Distributed on the Surface of the Studied Carbon Materials

	oxygen species [atom %]					nitrogen species [atom %]				
sample[a]	C═O	O═C−O	C−O	N−O	total O	pyridinic	pyrrolic	graphitic	oxidized	total N
S0	0.73	1.37	2.44	0.00	4.5					
S0_N	0.51	0.25	1.52	0.00	2.3	0.27	0.22	0.18	0.00	0.7
SK	3.01	4.32	2.49	3.54	13.4	0.17	0.53	0.09	1.81	2.6
SK_N	2.06	0.41	3.16	0.00	5.6	2.40	1.02	0.28	0.00	3.7
spent SK_N	1.85	2.91	6.45	0.00	11.2	0.44	0.61	0.32	0.20	1.6

[a]S0, SK, S0_N, and SK_N stand for unmodified carbon replica, carbon replica treated with HNO_3, carbon replica treated with NH_3, and car-bon replica treated first with HNO_3 and then NH_3.

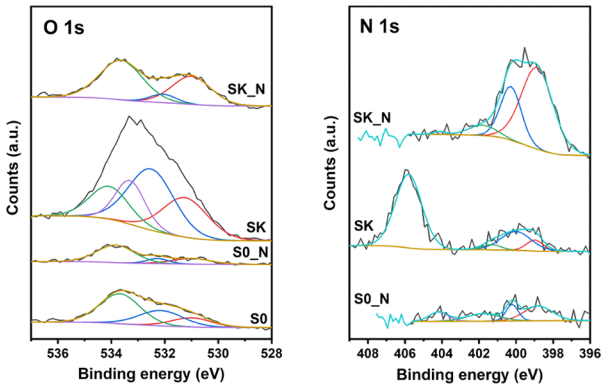

Figure 2. XPS O 1s and N 1s spectra of the pristine and modified mesoporous carbon replicas. S0, SK, S0_N, and SK_N stand for unmodified carbon replica, carbon replica treated with HNO_3, carbon replica treated with NH_3, and carbon replica treated first with HNO_3 and then NH_3.

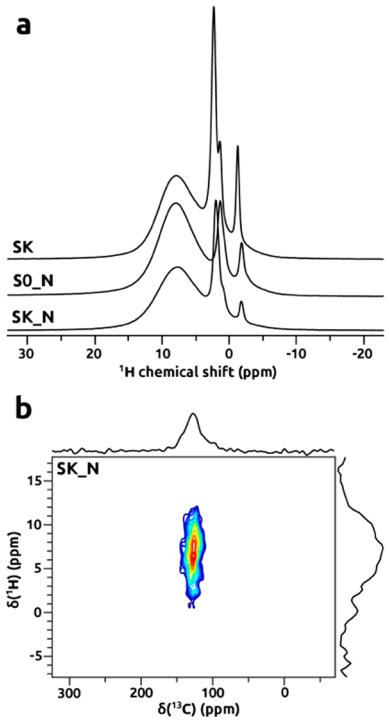

Figure 3. ^1H MAS NMR (a) and $^1H-^{13}C$ HETCOR (b) spectra collected from as indicated samples at 60 kHz MAS rate and magnetic field strength 14.1 T. SK, S0_N, and SK_N stand for carbon replica treated with HNO_3, carbon replica treated with NH_3, and carbon replica treated first with HNO_3 and then NH_3.

401.6 eV (±0.2 eV), and 405.8 eV (the latter one exceptionally for SK) were distinguished and attributed to pyridinic, pyrrolic, quaternary nitrogen, and oxidized nitrogen species, respectively.[60,61] In turn, in the O 1s spectra, three essential peaks appeared at 531.1 eV (±0.1 eV), 532.2 eV (±0.1 eV), and 533.8 eV (±0.1 eV) and were assigned to C═O (oxygen atom in carbonyl), O═C−O (oxygen atom in ester, anhydride and carboxylic acid), and C−O (oxygen atom in phenol/ether), respectively.[62,63] Furthermore, one more component was found at 533.3 eV for the HNO_3 treated sample (SK) and assigned to nitro groups.[64] Obviously, during the modification of SK with NH_3 (sample SK_N), the nitro species were reduced completely, forming mainly pyridinic and pyrrolic functionalities (cf. Table 2). Finally, in the SK_N sample with the highest amount of nitrogen (3.7 at. %), one could also observe significant changes in the distribution of the oxygen species. The performed modification led to the effective elimination of the carboxyl groups and prevented the relatively high contents of C═O and C−OH moieties observed for the SK material.

To obtain deeper insight into the surface composition of the carbon samples at the atomic level, solid-state NMR experiments were performed. In Figure 3A, ^1H MAS NMR spectra (60 kHz MAS) of SK, S0_N, and SK_N are presented. All samples exhibit a very similar pattern of proton signals, where a main, broad resonance (as a consequence of disorder) centered at 8 ppm represents the aromatic protons, and signals in the chemical shift range of 2−4 ppm can be assigned to protons in ethoxy and hydroxyl groups. There is also a signal with a rather unusual negative chemical shift in all three samples, which may be attributable to a so-called nucleus-independent chemical shift (NICS) effect on the protons of H_2O confined in the internal cavities of the doped carbon particles.[65,66] The fitted total amount of nonaromatic protons for each sample is 38.8% (SK sample), 24.1% (S0_N), and 29.8% (SK_N), whereas signal components with negative chemical shifts constitute 7.8% (SK), 6.5% (S0_N), and 4.1% (SK_N). Chemical shift differences among these signals result probably from changes in samples' texture (Table 1).

As revealed by the $^1H-^{13}C$ heteronuclear correlation (HETCOR) spectrum of the SK_N sample (Figure 3B), the broad signal due to the aromatic protons correlates with the ^{13}C resonance of graphitic carbons at ∼130 ppm, indicating that these protons terminate the edges of the doped carbon. Note that under these experimental conditions of 60 kHz MAS, both the chemical shift anisotropy (CSA) and dipolar resonance broadening are largely suppressed, and so neither contributes significantly to the ^{13}C line width; this line width (fwhm ∼25 ppm) can therefore be attributed solely to a chemical shift distribution due to structural disorder. To observe the full range of ^{13}C and ^{15}N environments, direct

https://dx.doi.org/10.1021/acs.chemmater.0c01666
Chem. Mater. 2020, 32, 7263−7273

excitation of a larger sample volume at 7 kHz MAS was also employed. In the directly excited ^{13}C MAS NMR spectrum of the SK_N sample (Figure 4A), the resonance of the sp^2

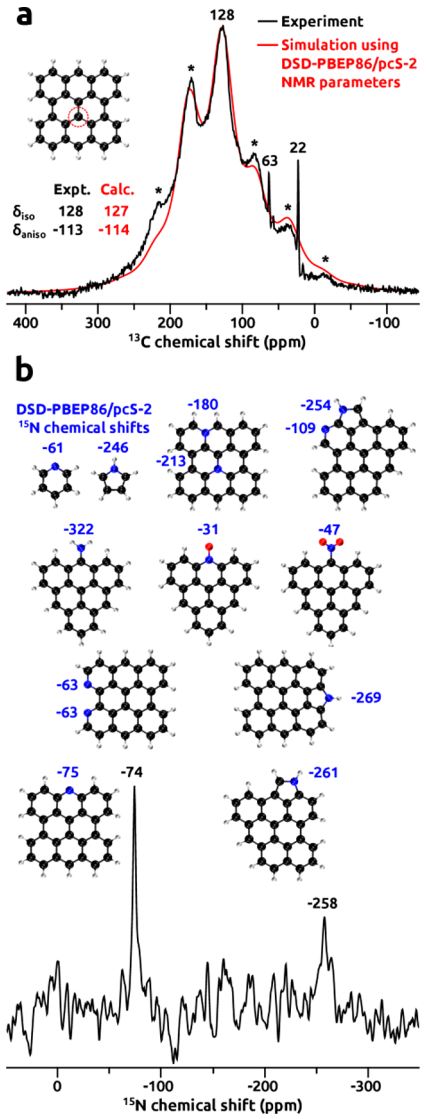

Figure 4. Directly excited ^{13}C (a) and ^{15}N (b) MAS NMR spectra of the SK_N sample collected at 7 kHz MAS and 14.1 T, shown together with chemical shifts calculated for hypothetical structural motifs. Experimental chemical shifts are given in black, calculated ^{13}C shifts are in red, and ^{15}N are in blue. All shifts are in ppm. The DFT-derived ^{13}C CSA parameters are $\eta = 0.23$, $\delta_{xx} = 197$, $\delta_{yy} = 171$, and $\delta_{zz} = 14$ ppm. SK_N stands for the carbon replica treated first with HNO_3 and then NH_3.

hybridized carbon atoms appears as a spinning sideband manifold with an isotropic chemical shift of 128 ppm and a CSA of −113 ppm. The estimated line width of the center band is similar to that of the ^{13}C projection of the HETCOR spectrum, which indicates structural disorder as a main source of broadening. In addition, we also see two minor signals at 63 and 22 ppm. The very narrow line widths of the these indicate fast dynamics, and therefore we attribute them to the mobile ethoxy groups linked to the carbon sheet via ether or ester groups, which is consistent with ^{1}H proton resonances in the range of 2−4 ppm (Figure 3A). Similar ^{13}C NMR shifts have been reported for graphite and graphene related materials.[67−70]

The ^{15}N MAS NMR spectrum of the same sample is presented in Figure 4B. Since no cross-polarization (CP) was used, all nitrogen moieties present in the structure should be detectable. Two distinct ^{15}N resonances are clearly identified: one at −74 ppm and another one at −258 ppm. These values fall in the shift ranges characteristic for pyridinic (−50 to −150 ppm) and pyrrolic (−200 to −270 ppm) nitrogen sites.[71]

To corroborate the NMR signal assignments and derive molecular representations of the local motifs present in the material, ^{13}C and ^{15}N NMR chemical shifts were calculated using quantum chemistry methods on a variety of structural models. The perturbatively corrected DSD-PBEP86 DFT approximation coupled with NMR-optimized pcS-*n* basis sets currently constitutes the most reliable and robust method for NMR shift prediction of main group elements.[51,72] The calculated ^{13}C isotropic chemical shift and CSA for the carbon atom (circled in red) in the graphene model of Figure 4A are in excellent agreement with the values obtained from the experimental spectrum of the SK_N sample. Therefore, it can be concluded that this local environment represents the majority of the carbon atoms in the sample with spectral broadening originating from structural disorder and that packing/$\pi-\pi$ stacking effects (if present) are minor, which is also corroborated by unaffected shifts of aromatic and ethoxy/hydroxyl protons. Several local environments of nitrogen atoms have been proposed and discussed in the literature on N-doped carbon materials.[37,73] We considered them herein by construction and evaluation of appropriate models, which are presented in Figure 4B. The only models that exhibit ^{15}N shifts that match the experimental spectrum are those with "pyridinic" nitrogen and "pyrrolic" nitrogen, in agreement with XPS. The sharp experimental peak at −74 ppm is consistent with only one structural model, which is that of pyridinic nitrogen sited at the edge of the carbon sheet (with a calculated shift of −75 ppm); hence we consider this resonance to represent only this type of pyridinic nitrogen. On the other hand, the interpretation of the broader resonance at −258 ppm requires more care, as it is consistent with three structural models of pyrrolic nitrogen with calculated shifts in the range −254 to −269 ppm: "external pyrrolic nitrogen" (−261 ppm), "edge pyrrolic nitrogen" (−269 ppm), and pyrrolic nitrogen two bonds two bonds from pyridinic nitrogen (−254 and −109 ppm respectively). Fortunately, some simplification in the assignment is possible. The presence of pyrrolic nitrogen two bonds from pyridinic nitrogen can be excluded due to the absence of a resonance close to −109 ppm, and the "edge pyrrolic nitrogen" can also be discounted due to the large mechanical strain required for a five-membered aromatic ring to form at the edge of the carbon sheet. Therefore, we ascribe this resonance solely to "external" pyrrolic nitrogen. The solid-state NMR results also exclude the presence of oxidized nitrogen, as no resonances are observed at −31 ppm (N═O) or −47 ppm (NO_2), again in agreement with XPS.

These results indicate that the nitrogen atoms are predominantly present at the carbon edges in the carbon replica treated first with HNO_3 and then NH_3. However, some comment is required to address the absence of any signals in the solid-state NMR spectrum corresponding to graphitic nitrogen, which appears to contradict the XPS results, which indicates that graphitic nitrogen is indeed present, albeit in lower amounts. This apparent contradiction can be resolved by the following observations. First, we note that the predicted

https://dx.doi.org/10.1021/acs.chemmater.0c01666
Chem. Mater. 2020, 32, 7263−7273

graphitic nitrogen chemical shifts depend strongly on the distance of the nitrogen from the edge, which would result in a broad resonance. Second, the low graphitic content (~25% compared to pyrrolic nitrogen) would result in inherently low sensitivity for this environment. Both observations indicate that the signals from such graphitic nitrogen environments, if present, are lost within the spectral noise due to the low signal-to-noise ratio of the experimental spectrum as a consequence of direct ^{15}N NMR detection at natural abundance.[74] Finally, we also note that none of the models with two nitrogens in close proximity (i.e., two/three bonds separation) gives a pair of shifts consistent with the experimental spectrum; therefore we can discount any significant clustering of the nitrogen on doping.

Electrochemical Removal of Nitrates. The selective doping of carbon materials with nitrogen atoms, i.e., the atomic control over the nitrogen distribution, is of high importance to tailor the electrocatalytic properties for several electrochemical reactions, such as the ORR or CO_2 reduction.[75,76] For instance, pyridinic N is considered the most active catalytic site in comparison to the pyrrolic or graphitic nitrogens for ORR.[77] Given the atomic resolution of the nitrogen positions within our carbon materials on the basis of ^{15}N solid state NMR experiments, we investigated the electrochemical reduction of nitrate on the nitrogen-free S0 carbon electrode and the SK_N carbon material containing nitrogen at the edge sites. In particular, we were interested in how the presence of nitrogen at these positions affected the selectivity of nitrate reduction toward either molecular nitrogen or NH_3.

Both the S0 and SK_N carbon-rich electrodes developed cathodic currents due to the hydrogen evolution reaction (HER) and showed a decrease in geometric current density when no nitrate was added to the solutions. This could be deduced from the linear square voltammetry (LSV) performed under near-neutral conditions for the S0 and SK_N electrodes in the absence and presence of nitrate, depicted in Figure 5. In

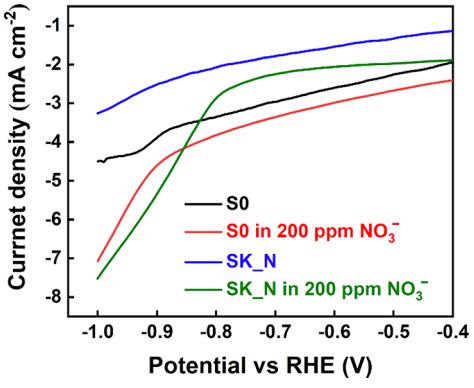

Figure 5. LSV curves of C and edge−N−C in 0.1 M Na_2SO_4 with the absence and presence of 200 ppm nitrate at a scan rate of 1 mV s^{-1}. Current densities relate to geometric current densities. S0 and SK_N stand for unmodified carbon replica and carbon replica treated first with HNO_3 and then NH_3.

the presence of nitrate, cathodic peaks are visible at −0.9 V vs RHE and −0.8 V vs RHE for both the S0 and SK_N electrode. This trend is visible also in the chronoamperometry (CA) recorded at −0.84 V vs RHE (Figure 6). Since the electrode preparation was identical for S0 and SK_N, the almost identical current density of −4 mA cm^{-2} at this potential value suggests no relevant influence of the (i) nitrogen positions

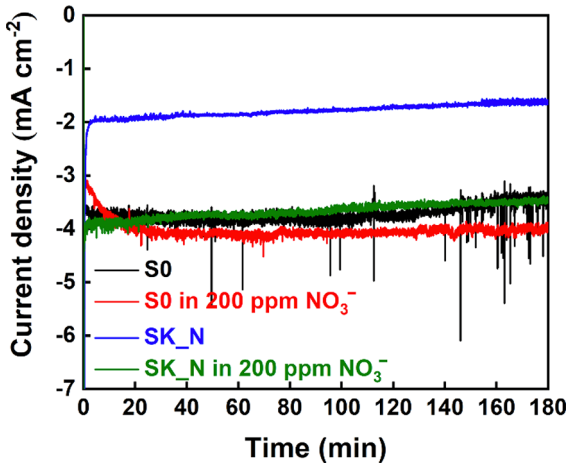

Figure 6. Constant potential electrolysis of C and edge−N−C at −0.84 V vs RHE in 0.1 M Na_2SO_4 with the absence and presence of 200 ppm nitrate. Current densities relate to geometric current densities. S0 and SK_N stand for an unmodified carbon replica and carbon replica treated first with HNO_3 and then NH_3, respectively.

within the carbon structure or (ii) the general presence of nitrogen in the carbon samples on the electrocatalytic activity. This was deduced from the trends in the chronoamperometry (CA) recorded at −0.84 V vs RHE (Figure 6).

To elucidate whether the generated electric current was used to reduce nitrate, we analyzed the nitrate, nitrite, and NH_3 concentration after 3 h of CA at this potential nitrite and NH_3 production (Table 3). The current density for nitrate reduction at −0.84 V vs RHE was almost identical for the bare carbon electrode (S0) and the electrode containing nitrogen atoms as dopants (SK_N). In combination with the structural analysis based on ^{15}N solid-state NMR, the electrochemical results showed that the nitrate reduction was independent of the presence and structural positions of the nitrogen atoms in the carbon material. Furthermore, the nitrogen doping did not influence the outcome of the observed selectivity. It should be noted that this effect may be changed for different electrochemical reactions, such as the nitrogen reduction reaction (NRR) or CO_2 reduction. However, these electrochemical results shed light on the reaction mechanism of nitrate reduction by proving that the selectivity did not depend on the presence of nitrogen atoms.

Oxidative Dehydrogenation of Ethylbenzene. The synthesized carbon materials were also tested in the oxidative dehydrogenation of ethylbenzene to determine an influence of the introduction of N into the edge positions on their catalytic activity. We decided to choose this pathway of transformation of EB into styrene, despite the fact that many recent reports have referred to the use of nitrogen-doped carbon materials in the direct dehydrogenation of EB.[24,62,63,78,79] The oxidative route allows to significantly reduce the process temperature and omit the thermodynamic limitations, and thus leads to greater economic opportunities to implement the developed technology.[80−82]

The studied carbon materials appeared to be very active and selective at a chosen temperature of 350 °C (Table 4). Apart from styrene (>94%), only small amounts of byproducts (mainly CO_2) were formed. Evidently, the initial catalytic activity and selectivity to the desired product increased on N doping. However, the best results were achieved over SK_N, which gave after 15 min time-on-stream an EB conversion as

https://dx.doi.org/10.1021/acs.chemmater.0c01666
Chem. Mater. 2020, 32, 7263−7273

Table 3. Electrochemical Reduction of Nitrate on S0 and SK_N Electrodes in 0.1 M Na_2SO_4 Electrolyte

electrode[a]	CA conditions	initial concentration of NO_3^- (ppm)	final concentration of NO_3^- (ppm)	reduction efficiency of NO_3^- (%)	final concentration of NO_2^- (ppm)	final concentration of NH_4^+ (ppm)	NO_3^- + NO_2^- + NH_4^+ (ppm)
S0	−0.843 V vs RHE for 3 h (pH 5.93)	200	105	47.5	5.8	11.0	121.8
SK_N	−0.843 V vs RHE for 3 h (pH 5.85)	200	103	48.5	8.4	9.7	121.1

[a]S0 and SK_N stand for an unmodified carbon replica and carbon replica treated first with HNO_3 and then NH_3.

Table 4. Conversion of EB and Selectivity to Styrene Achieved in the Oxidative Dehydrogenation of EB at 350 °C over the Studied Catalysts at the Beginning (15 min Time-on-Stream) and the End of Catalytic Run (360 min Time-on-Stream)

	EB conversion [%]		selectivity to styrene [%]	
catalyst[a]	15 min	360 min	15 min	360 min
S0	29.8 ± 1.2	17.2 ± 0.4	95.1 ± 0.1	94.2 ± 0.1
S0_N	33.4 ± 1.4	16.2 ± 0.4	98.0 ± 0.1	96.8 ± 0.1
SK	34.0 ± 1.4	14.1 ± 0.4	96.1 ± 0.1	96.0 ± 0.1
SK_N	38.7 ± 1.6	19.2 ± 0.5	96.3 ± 0.1	96.6 ± 0.1

[a]S0, SK, S0_N, and SK_N stand for unmodified carbon replica, carbon replica treated with HNO_3, carbon replica treated with NH_3, and carbon replica treated first with HNO_3 and then NH_3.

high as 38.7% with a selectivity toward styrene of 96.3%. During the catalytic runs, all studied catalysts lost gradually their initial activity due to coke deposition, which is a typical side reaction observed in the dehydrogenation of alkanes even under an oxidizing atmosphere. Nevertheless, the SK_N catalyst still showed 19.2% of the EB conversion after 6 h of the reaction (when the catalytic performance is stabilized) with the selectivity to styrene (96.6%) close to the initial value. Interesting information on the state of the surface of the SK_N sample after the reaction is provided by XPS measurements (Table 2). The formed carbon deposit significantly reduced the availability of pyridinic and pyrrole groups while maintaining the content of graphitic species. Apparently, the coke covered preferentially the N5 and N6 centers. On the other hand, the formed carbon deposit was highly oxidized. The content of oxygen-containing functionalities in the SK_N sample after the catalytic test almost doubled compared to the fresh material. Particularly, the concentration of ester, anhydride, carboxylic acid, and/or phenol groups increased, and even reduction in the content of carbonyl species was observed.

The catalytic role of the N-containing groups in the oxidative dehydrogenation of alkanes was attributed to activation of the O_2 molecule, which is suggested to be most efficient at graphitic nitrogen sites.[61,83] The calculations showed that a difference in electronegativity causes a transfer of electrons from C atoms to graphitic N atoms obtaining a positive charge and becoming adsorption sites for oxygen molecules. On the other hand, it was found that N doping facilitates C−H breaking in an alkane molecule and desorption of a resulting alkene molecule.[84] Nevertheless, Pelech et al.[85] did not observe any correlation between a content of quaternary nitrogen in N-doped carbon xerogels and their catalytic activity in the oxidative dehydrogenation of isobutene. A clear relationship was found for the total nitrogen content. Our study based on the application of ^{15}N solid-state NMR and XPS clarifies this finding. The catalytic effect of N species in the oxidative dehydrogenation processes should rather correspond to their presence at the edge sites. However, it should be kept in mind that other factors also determine the catalytic activity of these materials. In our case, the modification procedure resulted in a partial destruction of perfect spherical morphology, giving a higher porosity (including an expanded surface area) and accessibility of reacting molecules to the active sites. However, the influence of these morphological changes is difficult to assess and differentiate from those related to the N-doping at the current state. Additionally, high disorder of the carbon structure (confirmed by Raman spectroscopy) and significant elimination of COOH groups combined with exposition of C═O/C−O ones (revealed by XPS) could potentially have a beneficial effect for the initial catalytic activity by facilitating abstraction of hydrogen atoms from the ethylbenzene molecule on the surface sites.[86,87]

CONCLUSION

^{15}N solid-state nuclear magnetic resonance spectroscopy was proven to be an excellent tool to recognize the type of N species being generated on the surface of a mesoporous carbon replica. Furthermore, theoretical considerations showed the detailed location of the N atoms in the carbon structure. For the material synthesized by nanoreplication of a silica template using sucrose as a carbon source, modification based on a contact with HNO_3 solution followed by a treatment in gaseous NH_3 at elevated temperature appeared to be the most efficient way to form a high amount of pyridinic N at the edge and pyrrolic N external to the edge. The presence of these moieties did not influence significantly the electrochemical activity in NO_3^- elimination but was important for the observed improved catalytic performance in the oxidative dehydrogenation of ethylbenzene for the N-rich carbon catalysts. The developed N-loaded carbon catalyst with spherical morphology (confirmed by SEM), expanded mesopore system (N_2 adsorption), suitable graphitization (XRD, Raman spectroscopy), and tuned C═O/C−OH distribution on the surface (XPS), produced by using the simple and inexpensive procedure, could be a relevant candidate for further studies toward commercial applications.

AUTHOR INFORMATION

Corresponding Authors

Adam Slabon − *Department of Materials and Environmental Chemistry, Stockholm University, 106 91 Stockholm, Sweden;* orcid.org/0000-0002-4452-1831; Email: adam.slabon@mmk.su.se

Piotr Kuśtrowski − *Faculty of Chemistry, Jagiellonian University, 30-387 Kraków, Poland*; Email: piotr.kustrowski@uj.edu.pl

https://dx.doi.org/10.1021/acs.chemmater.0c01666
Chem. Mater. 2020, 32, 7263−7273

Authors

Ireneusz Szewczyk − *Faculty of Chemistry, Jagiellonian University, 30-387 Kraków, Poland*

Anna Rokicińska − *Faculty of Chemistry, Jagiellonian University, 30-387 Kraków, Poland*

Marek Michalik − *Institute of Geological Science, Faculty of Geography and Geology, Jagiellonian University, 30-387 Kraków, Poland*

Jianhong Chen − *Department of Materials and Environmental Chemistry, Stockholm University, 106 91 Stockholm, Sweden*

Aleksander Jaworski − *Department of Materials and Environmental Chemistry, Stockholm University, 106 91 Stockholm, Sweden;* orcid.org/0000-0002-7156-559X

Rihards Aleksis − *Department of Materials and Environmental Chemistry, Stockholm University, 106 91 Stockholm, Sweden*

Andrew J. Pell − *Department of Materials and Environmental Chemistry, Stockholm University, 106 91 Stockholm, Sweden;* orcid.org/0000-0002-2542-8113

Niklas Hedin − *Department of Materials and Environmental Chemistry, Stockholm University, 106 91 Stockholm, Sweden;* orcid.org/0000-0002-7284-2974

Complete contact information is available at: https://pubs.acs.org/10.1021/acs.chemmater.0c01666

Author Contributions

All authors have given approval to the final version of the manuscript.

Notes

The authors declare no competing financial interest.

■ ACKNOWLEDGMENTS

The XPS measurements were carried out with the equipment purchased with the financial support of the European Regional Development Fund in the framework of the Polish Innovation Operational Program (contract no. POIG.02.01.00-12-023/08). A.S. acknowledges MISTRA (project: *SafeChem*) for financial support. A.J., R.A., and A.J.P. were supported by the Swedish Research Council (project no. 2016-03441). The authors thank Dr. Serhiy Budnyk and AC2T research GmbH for ICP analysis.

■ REFERENCES

(1) Zhang, Z.; Feng, X.; Yue, X. X.; An, F. Q.; Zhou, W. X.; Gao, J. F.; Hu, T. P.; Wei, C. C. Effective Adsorption of Phenols Using Nitrogen-Containing Porous Activated Carbon Prepared from Sunflower Plates. *Korean J. Chem. Eng.* **2015**, *32*, 1564−1569.

(2) Plaza, M. G.; Pevida, C.; Arenillas, A.; Rubiera, F.; Pis, J. J. CO_2 Capture by Adsorption with Nitrogen Enriched Carbons. *Fuel* **2007**, *86*, 2204−2212.

(3) Ma, R.; Lin, G.; Zhou, Y.; Liu, Q.; Zhang, T.; Shan, G.; Yang, M.; Wang, J. A Review of Oxygen Reduction Mechanisms for Metal-Free Carbon-Based Electrocatalysts. *npj Comput. Mater.* **2019**, *5*, 5.

(4) Guo, D.; Shibuya, R.; Akiba, C.; Saji, S.; Kondo, T.; Nakamura, J. Active Sites of Nitrogen-Doped Carbon Materials for Oxygen Reduction Reaction Clarified Using Model Catalysts. *Science* **2016**, *351*, 361−365.

(5) Hu, E.; Yu, X. Y.; Chen, F.; Wu, Y.; Hu, Y.; Lou, X. W. D. Graphene Layers-Wrapped Fe/Fe_5C_2 Nanoparticles Supported on N-Doped Graphene Nanosheets for Highly Efficient Oxygen Reduction. *Adv. Energy Mater.* **2018**, *8*, 1−8.

(6) Liu, R.; Wu, D.; Feng, X.; Müllen, K. Nitrogen-Doped Ordered Mesoporous Graphitic Arrays with High Electrocatalytic Activity for Oxygen Reduction. *Angew. Chem., Int. Ed.* **2010**, *49*, 2565−2569.

(7) Jiao, Y.; Zheng, Y.; Jaroniec, M.; Qiao, S. Z. Design of Electrocatalysts for Oxygen- and Hydrogen-Involving Energy Conversion Reactions. *Chem. Soc. Rev.* **2015**, *44*, 2060−2086.

(8) Mamtani, K.; Jain, D.; Zemlyanov, D.; Celik, G.; Luthman, J.; Renkes, G.; Co, A. C.; Ozkan, U. S. Probing the Oxygen Reduction Reaction Active Sites over Nitrogen-Doped Carbon Nanostructures (CN_x) in Acidic Media Using Phosphate Anion. *ACS Catal.* **2016**, *6*, 7249−7259.

(9) Budnyak, T. M.; Slabon, A.; Sipponen, M. H. Lignin-Inorganic Interfaces: Chemistry and Applications from Adsorbents to Catalysts and Energy Storage Materials, *ChemSusChem* **2020**, in press, DOI: 10.1002/cssc.202000216.

(10) Maldonado, S.; Morin, S.; Stevenson, K. J. Structure, Composition, and Chemical Reactivity of Carbon Nanotubes by Selective Nitrogen Doping. *Carbon* **2006**, *44*, 1429−1437.

(11) Han, M.; Zhu, S.; Lu, S.; Song, Y.; Feng, T.; Tao, S.; Liu, J.; Yang, B. Recent Progress on the Photocatalysis of Carbon Dots: Classification, Mechanism and Applications. *Nano Today* **2018**, *19*, 201−218.

(12) Ma, Z.; Zhang, H.; Yang, Z.; Ji, G.; Yu, B.; Liu, X.; Liu, Z. Mesoporous Nitrogen-Doped Carbons with High Nitrogen Contents and Ultrahigh Surface Areas: Synthesis and Applications in Catalysis. *Green Chem.* **2016**, *18*, 1976−1982.

(13) Friedel Ortega, K.; Arrigo, R.; Frank, B.; Schlögl, R.; Trunschke, A. Acid-Base Properties of N-Doped Carbon Nanotubes: A Combined Temperature-Programmed Desorption, X-Ray Photoelectron Spectroscopy, and 2-Propanol Reaction Investigation. *Chem. Mater.* **2016**, *28*, 6826−6839.

(14) Frank, B.; Rinaldi, A.; Blume, R.; Schlögl, R.; Su, D. S. Oxidation Stability of Multiwalled Carbon Nanotubes for Catalytic Applications. *Chem. Mater.* **2010**, *22*, 4462−4470.

(15) Sun, X. Y.; Li, B.; Su, D. Revealing the Nature of the Active Site on the Carbon Catalyst for C-H Bond Activation. *Chem. Commun.* **2014**, *50*, 11016−11019.

(16) Ryoo, R.; Joo, S. H.; Jun, S. Synthesis of Highly Ordered Carbon Molecular Sieves via Template-Mediated Structural Transformation. *J. Phys. Chem. B* **1999**, *103*, 7743−7746.

(17) Zhao, Z.; Dai, Y.; Lin, J.; Wang, G. Highly-Ordered Mesoporous Carbon Nitride with Ultrahigh Surface Area and Pore Volume as a Superior Dehydrogenation Catalyst. *Chem. Mater.* **2014**, *26*, 3151−3161.

(18) Agresti, F.; Barison, S.; Famengo, A.; Pagura, C.; Fedele, L.; Rossi, S.; Bobbo, S.; Rancan, M.; Fabrizio, M. Surface Oxidation of Single Wall Carbon Nanohorns for the Production of Surfactant Free Water-Based Colloids. *J. Colloid Interface Sci.* **2018**, *514*, 528−533.

(19) Li, J.; Yu, P.; Xie, J.; Liu, J.; Wang, Z.; Wu, C.; Rong, J.; Liu, H.; Su, D. Improving the Alkene Selectivity of Nanocarbon-Catalyzed Oxidative Dehydrogenation of n-Butane by Refinement of Oxygen Species. *ACS Catal.* **2017**, *7*, 7305−7311.

(20) Cordero-Lanzac, T.; Rosas, J. M.; García-Mateos, F. J.; Ternero-Hidalgo, J. J.; Palomo, J.; Rodríguez-Mirasol, J.; Cordero, T. Role of Different Nitrogen Functionalities on the Electrochemical Performance of Activated Carbons. *Carbon* **2018**, *126*, 65−76.

(21) Kwon, H. C.; Yook, S.; Choi, S.; Choi, M. Comprehensive Understanding of the Effects of Carbon Nanostructures on Redox Catalytic Properties and Stability in Oxidative Dehydrogenation. *ACS Catal.* **2017**, *7*, 5257−5267.

(22) Yu, D.; Wei, L.; Jiang, W.; Wang, H.; Sun, B.; Zhang, Q.; Goh, K.; Si, R.; Chen, Y. Nitrogen Doped Holey Graphene as an Efficient Metal-Free Multifunctional Electrochemical Catalyst for Hydrazine Oxidation and Oxygen Reduction. *Nanoscale* **2013**, *5*, 3457−3464.

(23) Arrigo, R.; Hävecker, M.; Wrabetz, S.; Blume, R.; Lerch, M.; McGregor, J.; Parrott, E. P. J.; Zeitler, J. A.; Gladden, L. F.; Knop-Gericke, A.; Schlogl, R.; Su, D. S. Tuning the Acid/Base Properties of Nanocarbons by Functionalization via Amination. *J. Am. Chem. Soc.* **2010**, *132*, 9616−9630.

(24) Ba, H.; Liu, Y.; Truong-Phuoc, L.; Duong-Viet, C.; Nhut, J. M.; Nguyen, D. L.; Ersen, O.; Tuci, G.; Giambastiani, G.; Pham-Huu, C.

N-Doped Food-Grade-Derived 3D Mesoporous Foams as Metal-Free Systems for Catalysis. *ACS Catal.* **2016**, *6*, 1408−1419.
(25) Cazetta, A. L.; Zhang, T.; Silva, T. L.; Almeida, V. C.; Asefa, T. Bone Char-Derived Metal-Free N- and S-Co-Doped Nanoporous Carbon and Its Efficient Electrocatalytic Activity for Hydrazine Oxidation. *Appl. Catal., B* **2018**, *225*, 30−39.
(26) Kiciński, W.; Szala, M.; Bystrzejewski, M. Sulfur-Doped Porous Carbons: Synthesis and Applications. *Carbon* **2014**, *68*, 1−32.
(27) Palomo, J.; Ternero-Hidalgo, J. J.; Rosas, J. M.; Rodríguez-Mirasol, J.; Cordero, T. Selective Nitrogen Functionalization of Phosphorus-Containing Activated Carbons. *Fuel Process. Technol.* **2017**, *156*, 438−445.
(28) Fujita, S. I.; Watanabe, H.; Katagiri, A.; Yoshida, H.; Arai, M. Nitrogen and Oxygen-Doped Metal-Free Carbon Catalysts for Chemoselective Transfer Hydrogenation of Nitrobenzene, Styrene, and 3-Nitrostyrene with Hydrazine. *J. Mol. Catal. A: Chem.* **2014**, *393*, 257−262.
(29) Zimmerman, J. B.; Anastas, P. T.; Erythropel, H. C.; Leitner, W. Designing for a green chemistry future. *Science* **2020**, *367*, 397−400.
(30) Qi, W.; Yan, P.; Su, D. S. Oxidative Dehydrogenation on Nanocarbon: Insights into the Reaction Mechanism and Kinetics via in Situ Experimental Methods. *Acc. Chem. Res.* **2018**, *51*, 640−648.
(31) Liu, W.; Wang, C.; Su, D.; Qi, W. Oxidative Dehydrogenation of Ethylbenzene on Nanocarbon: Kinetics and Reaction Mechanism. *J. Catal.* **2018**, *368*, 1−7.
(32) Strelko, V. V.; Kuts, V. S.; Thrower, P. A. On the Mechanism of Possible Influence of Heteroatoms of Nitrogen, Boron and Phosphorus in a Carbon Matrix on the Catalytic Activity of Carbons in Electron Transfer Reactions. *Carbon* **2000**, *38*, 1499−1503.
(33) Seo, S.; Yoon, Y.; Lee, J.; Park, Y.; Lee, H. Nitrogen-Doped Partially Reduced Graphene Oxide Rewritable Nonvolatile Memory. *ACS Nano* **2013**, *7*, 3607−3615.
(34) Shafeeyan, M. S.; Daud, W. M. A. W.; Houshmand, A.; Arami-Niya, A. Ammonia Modification of Activated Carbon to Enhance Carbon Dioxide Adsorption: Effect of Pre-Oxidation. *Appl. Surf. Sci.* **2011**, *257*, 3936−3942.
(35) Ternero-Hidalgo, J. J.; Rosas, J. M.; Palomo, J.; Valero-Romero, M. J.; Rodríguez-Mirasol, J.; Cordero, T. Functionalization of Activated Carbons by HNO_3 Treatment: Influence of Phosphorus Surface Groups. *Carbon* **2016**, *101*, 409−419.
(36) Chisaka, M.; Iijima, T.; Ishihara, Y.; Suzuki, Y.; Inada, R.; Sakurai, Y. Carbon Catalyst Codoped with Boron and Nitrogen for Oxygen Reduction Reaction in Acid Media. *Electrochim. Acta* **2012**, *85*, 399−410.
(37) Kuroki, S.; Hosaka, Y.; Yamauchi, C. A Solid-State NMR Study of the Carbonization of Polyaniline. *Carbon* **2013**, *55*, 160−167.
(38) Wang, M.; Liu, S.; Qian, T.; Liu, J.; Zhou, J.; Ji, H.; Xiong, J.; Zhong, J.; Yan, C. Over 56.55% Faradaic Efficiency of Ambient Ammonia Synthesis Enabled by Positively Shifting the Reaction Potential. *Nat. Commun.* **2019**, *10*, 1−8.
(39) Hwang, T. L.; van Zijl, P. C. M.; Garwood, M. Fast Broadband Inversion by Adiabatic Pulses. *J. Magn. Reson.* **1998**, *133*, 200−203.
(40) Kervern, G.; Pintacuda, G.; Emsley, L. Fast Adiabatic Pulses for Solid-State NMR of Paramagnetic Systems. *Chem. Phys. Lett.* **2007**, *435*, 157−162.
(41) Neese, F. The ORCA Program System. *Wiley Interdiscip. Rev.: Comput. Mol. Sci.* **2012**, *2*, 73−78.
(42) Handy, N. C.; Cohen, A. J. Left-Right Correlation Energy. *Mol. Phys.* **2001**, *99*, 403−412.
(43) Lee, C.; Yang, W.; Parr, R. G. Development of the Colle-Salvetti Correlation-Energy Formula Into a Functional of the Electron Density. *Phys. Rev. B: Condens. Matter Mater. Phys.* **1988**, *37*, 785−789.
(44) Grimme, S.; Antony, J.; Ehrlich, S.; Krieg, H. A Consistent and Accurate Ab Initio Parametrization of Density Functional Dispersion Correction (DFT-D) for the 94 Elements H-Pu. *J. Chem. Phys.* **2010**, *132*, 154104.
(45) Grimme, S.; Ehrlich, S.; Goerigk, L. Effect of the Damping Function in Dispersion Corrected Density Functional Theory. *J. Comput. Chem.* **2011**, *32*, 1456−1465.
(46) Jensen, F. Unifying General and Segmented Contracted Basis Sets. Segmented Polarization Consistent Basis Sets. *J. Chem. Theory Comput.* **2014**, *10*, 1074−1085.
(47) Kozuch, S.; Martin, J. M. L. DSD-PBEP86: In Search of the Best Double-Hybrid DFT with Spin-Component Scaled MP2 and Dispersion Corrections. *Phys. Chem. Chem. Phys.* **2011**, *13*, 20104−20107.
(48) Jensen, F. Segmented Contracted Basis Sets Optimized for Nuclear Magnetic Shielding. *J. Chem. Theory Comput.* **2015**, *11*, 132−138.
(49) Weigend, F. Accurate Coulomb-fitting Basis Sets for H to Rn. *Phys. Chem. Chem. Phys.* **2006**, *8*, 1057−1065.
(50) Hättig, C. Optimization of Auxiliary Basis Sets for RI-MP2 and RI-CC2 Calculations: Core-Valence and Quintuple-Zeta Basis Sets for H to Ar and QZVPP Basis Sets for Li to Kr. *Phys. Chem. Chem. Phys.* **2005**, *7*, 59−66.
(51) Rzepka, P.; Bacsik, Z.; Pell, A. J.; Hedin, N.; Jaworski, A. Nature of Chemisorbed CO_2 in Zeolite A. *J. Phys. Chem. C* **2019**, *123*, 21497−21503.
(52) Chatt, J.; Fakley, M. E.; Richards, R. L.; Mason, J.; Stenhouse, I. A. Nitrogen-15 Magnetic Resonance Spectroscopic Studies of Dinitrogen Complexes of Molybdenum and Tungsten. *J. Chem. Research (S)* **1979**, 44−45.
(53) Robarge, W. P.; Edwards, A.; Johnson, B. Water and Waste Water Analysis for Nitrate via Nitration of Salicylic Acid. *Commun. Soil Sci. Plant Anal.* **1983**, *14*, 1207−1215.
(54) Zhao, Y.; Shi, R.; Bian, X.; Zhou, C.; Zhao, Y.; Zhang, S.; Wu, F.; Waterhouse, G. I. N.; Wu, L. Z.; Tung, C. H.; Zhang, T. Ammonia Detection Methods in Photocatalytic and Electrocatalytic Experiments: How to Improve the Reliability of NH_3 Production Rates? *Adv. Sci.* **2019**, *6*, 1802109.
(55) Sharma, P. P.; Wu, J.; Yadav, R. M.; Liu, M.; Wright, C. J.; Tiwary, C. S.; Yakobson, B. I.; Lou, J.; Ajayan, P. M.; Zhou, D. Nitrogen-Doped Carbon Nanotube Arrays for High - Efficiency Electrochemical Reduction of CO_2: on the Understanding of Defects, Defect Density, and Selectivity. *Angew. Chem., Int. Ed.* **2015**, *54*, 13701−13705.
(56) Ferrari, A. C. Raman Spectroscopy of Graphene and Graphite: Disorder, Electron−Phonon Coupling, Doping and Nonadiabatic Effects. *Solid State Commun.* **2007**, *143*, 47−57.
(57) Zhong, S.; Zhan, C.; Cao, D. Zeolitic Imidazolate Framework-Derived Nitrogen-Doped Porous Carbons as High Performance Supercapacitor Electrode Materials. *Carbon* **2015**, *85*, 51−59.
(58) Liu, Y.; Su, Y.; Quan, X.; Fan, X.; Chen, S.; Yu, H.; Zhao, H.; Zhang, Y.; Zhao, J. Facile Ammonia Synthesis from Electrocatalytic N_2 Reduction Under Ambient Conditions on N-doped Porous Carbon. *ACS Catal.* **2018**, *8*, 1186−1191.
(59) Ma, Z.; Thersleff, T.; Görne, A. L.; Cordes, N.; Liu, Y.; Jakobi, S.; Rokicinska, A.; Schichtl, Z. G.; Coridan, R. H.; Kustrowski, P.; Schnick, W.; Dronskowski, R.; Slabon, A. Quaternary Core-Shell Oxynitride Nanowire Photoanode Containing a Hole-Extraction Gradient for Photoelectrochemical Water Oxidation. *ACS Appl. Mater. Interfaces* **2019**, *11*, 19077−190865.
(60) Song, Y.; Liu, G.; Yuan, Z. Y. N-, P- and B-doped Mesoporous Carbons for Direct Dehydrogenation of Propane. *RSC Adv.* **2016**, *6*, 94636−94642.
(61) Cao, Y.; Mao, S.; Li, M.; Chen, Y.; Wang, Y. Metal/Porous Carbon Composites for Heterogeneous Catalysis: Old Catalysts with Improved Performance Promoted by N-Doping. *ACS Catal.* **2017**, *7*, 8090−8112.
(62) Tian, S.; Yan, P.; Li, F.; Zhang, X.; Su, D.; Qi, W. Fabrication of Polydopamine Modified Carbon Nanotube Hybrids and their Catalytic Activity in Ethylbenzene Dehydrogenation. *ChemCatChem* **2019**, *11*, 2073−2078.

https://dx.doi.org/10.1021/acs.chemmater.0c01666
Chem. Mater. 2020, 32, 7263−7273

(63) Qin, L.; Wang, L.; Wang, C.; Yang, X.; Lv, B. Enhanced Role of Graphitic-N on Nitrogen-Doped Porous Carbon Ball for Direct Dehydrogenation of Ethylbenzene. *Mol. Catal.* **2019**, *462*, 61−68.
(64) Zhang, B.; Yan, J.; Li, G.; Wang, Z. Carboxyl-, Hydroxyl-, and Nitro-Functionalized Porous Polyaminals for Highly Selective CO_2 Capture. *ACS Appl. Polym. Mater.* **2019**, *1*, 1524−1531.
(65) Forse, A. C.; Griffin, J. M.; Presser, V.; Gogotsi, Y.; Grey, C. P. Ring Current Effects: Factors Affecting the NMR Chemical Shift of Molecules Adsorbed on Porous Carbons. *J. Phys. Chem. C* **2014**, *118*, 7508−7514.
(66) Cervini, L.; Lynes, O. D.; Akien, G. R.; Kerridge, A.; Barrow, N. S.; Griffin, J. M. Factors Affecting the Nucleus- Independent Chemical Shift in NMR Studies of Microporous Carbon Electrode Materials. *Energy Storage Materials* **2019**, *21*, 335−346.
(67) Lerf, A.; He, H.; Riedl, T.; Forster, M.; Klinowski, J. ^{13}C and ^{1}H MAS NMR Studies of Graphite Oxide and its Chemically Modified Derivatives. *Solid State Ionics* **1997**, *101*, 857−862.
(68) Lerf, A.; He, H.; Forster, M.; Klinowski, J. Structure of Graphite Oxide Revisited. *J. Phys. Chem. B* **1998**, *102*, 4477−4482.
(69) Li, Y.; Chen, H.; Voo, L. Y.; Ji, J.; Zhang, G.; Zhang, G.; Zhang, F.; Fan, X. Synthesis of Partially Hydrogenated Graphene and Brominated Graphene. *J. Mater. Chem.* **2012**, *22*, 15021−15024.
(70) Zhang, Q.; Scrafford, K.; Li, M.; Cao, Z.; Xia, Z.; Ajayan, P. M.; Wei, B. Anomalous Capacitive Behaviors of Graphene Oxide Based Solid-State Supercapacitors. *Nano Lett.* **2014**, *14*, 1938−1943.
(71) Kelemen, S. R.; Afeworki, M.; Gorbaty, M. L.; Kwiatek, P. J.; Solum, M. S.; Hu, J. Z.; Pugmire, R. J. XPS and ^{15}N NMR Study of Nitrogen Forms in Carbonaceous Solids. *Energy Fuels* **2002**, *16*, 1507−1515.
(72) Stoychev, G. L.; Auer, A. A.; Neese, F. Efficient and Accurate Prediction of Nuclear Magnetic Resonance Shielding Tensors with Double-Hybrid Density Functional Theory. *J. Chem. Theory Comput.* **2018**, *14*, 4756−4771.
(73) Wu, G.; Santandreu, A.; Kellogg, W.; Gupta, S.; Ogoke, O.; Zhang, H.; Wang, H. L.; Dai, L. Carbon Nanocomposite Catalysts for Oxygen Reduction and Evolution Reactions: From Nitrogen Doping to Transition-Metal Addition. *Nano Energy* **2016**, *29*, 83−110.
(74) Fang, X. W.; Mao, J. D.; Levin, E. M.; Schmidt-Rohr, K. Nonaromatic Core-Shell Structure of Nanodiamond from Solid-State NMR Spectroscopy. *J. Am. Chem. Soc.* **2009**, *131*, 1426−1435.
(75) Wang, H.; Jia, J.; Song, P.; Wang, Q.; Li, D.; Min, S.; Qian, C.; Wang, L.; Li, Y. F.; Ma, C.; Wu, T.; Yuan, J.; Antonietti, M.; Ozin, G. A. Efficient Electrocatalytic Reduction of CO_2 by Nitrogen-Doped Nanoporous Carbon/Carbon Nanotube Membranes: A Step Towards the Electrochemical CO_2 Refinery. *Angew. Chem., Int. Ed.* **2017**, *56*, 7847−7852.
(76) Gong, K.; Du, F.; Xia, Z.; Durstock, M.; Dai, L. Nitrogen-Doped Carbon Nanotube Arrays with High Electrocatalytic Activity for Oxygen Reduction. *Science* **2009**, *323*, 760−764.
(77) Lv, Q.; Si, W.; He, J.; Sun, L.; Zhang, C.; Wang, N.; Yang, Z.; Li, X.; Wang, X.; Deng, W.; Long, Y.; Huang, C.; Li, Y. Selectively Nitrogen-Doped Carbon Materials as Superior Metal-Free Catalysts for Oxygen Reduction. *Nat. Commun.* **2018**, *9*, 3376.
(78) Ge, G.; Liu, H.; Zhao, Z. Three-Dimensional Interconnected Porous Nitrogen-Doped Carbon Hybrid Foam for Notably Promoted Direct Dehydrogenation of Ethylbenzene to Styrene. *ChemCatChem* **2019**, *11*, 4830−4840.
(79) Liu, Y.; Ba, H.; Luo, J.; Wu, K. H.; Nhut, J. M.; Su, D. S.; Pham-Huu, C. Structure-performance Relationship of Nanodiamonds @ Nitrogen-doped Mesoporous Carbon in the Direct Dehydrogenation of Ethylbenzene. *Catal. Today* **2018**, *301*, 38−47.
(80) Jarczewski, S.; Drozdek, M.; Michorczyk, P.; Cuadrado-Collados, C.; Gandara-Loe, J.; Silvestre-Albero, J.; Kuśtrowski, P. Oxidative Dehydrogenation of Ethylbenzene over CMK-1 and CMK-3 Carbon Replicas with Various Mesopore Architectures. *Microporous Mesoporous Mater.* **2018**, *271*, 262−272.
(81) Niebrzydowska, P.; Janus, R.; Kuśtrowski, P.; Jarczewski, S.; Wach, A.; Silvestre-Albero, A. M.; Rodríguez-Reinoso, F. A Simplified Route to the Synthesis of CMK-3 Replica Based on Precipitation Polycondensation of Furfuryl Alcohol in SBA-15 Pore System. *Carbon* **2013**, *64*, 252−261.
(82) Janus, P.; Janus, R.; Dudek, B.; Drozdek, M.; Silvestre-Albero, A.; Rodríguez-Reinoso, F.; Kuśtrowski, P. On Mechanism of Formation of SBA-15/Furfuryl Alcohol-Derived Mesoporous Carbon Replicas and its Relationship with Catalytic Activity in Oxidative Dehydrogenation of Ethylbenzene. *Microporous Mesoporous Mater.* **2020**, *299*, 110118.
(83) Chen, C.; Zhang, J.; Zhang, B.; Yu, C.; Peng, F.; Su, D. Revealing the Enhanced Catalytic Activity of Nitrogen-doped Carbon Nanotubes for Oxidative Dehydrogenation of Propane. *Chem. Commun.* **2013**, *49*, 8151−8153.
(84) Sun, X. Y.; Han, P.; Li, B.; Mao, S. J.; Liu, T. F.; Ali, S.; Lian, Z.; Su, D. S. Oxidative Dehydrogenation Reaction of Short Alkanes on Nanostructured Carbon Catalysts: a Computational Account. *Chem. Commun.* **2018**, *54*, 864−875.
(85) Pelech, I.; Soares, O. S. G. P.; Pereira, M. F. R.; Figueiredo, J. L. Oxidative Dehydrogenation of Isobutane on Carbon Xerogel Catalysts. *Catal. Today* **2015**, *249*, 176−183.
(86) Grant, J. T.; Carrero, C. A.; Goeltl, F.; Venegas, J.; Mueller, P.; Burt, S. P.; Specht, S. E.; McDermott, W. P.; Chieregato, A.; Hermans, I. Selective oxidative dehydrogenation of propane to propene using boron nitride catalysts. *Science* **2016**, *354*, 1570−1573.
(87) Mestl, G.; Maksimova, N. I.; Keller, N.; Roddatis, V. V.; Schlögl, R. Carbon Nanofilaments in Heterogeneous Catalysis: An Industrial Application for New Carbon Materials? *Angew. Chem., Int. Ed.* **2001**, *40*, 2066−2068.

https://dx.doi.org/10.1021/acs.chemmater.0c01666
Chem. Mater. 2020, 32, 7263−7273